The X-pattern Merging of the Equatorial Ionization Anomaly Crests

F. I. Laskar[1], D. K. Karan[1], R. E. Daniell[2], M. V. Codrescu[3], R. W. Eastes[1], N. M. Pedatella[4], W. Wang[4], A. Maute[3,5], P. K. Rajesh[6], W. E. McClintock[1]

[1]Laboratory for Atmospheric and Space Physics, University of Colorado, Boulder, CO, USA
[2]Ionospheric Physics Consulting, Stoughton, MA, USA
[3]Space Weather Prediction Center, NOAA, Boulder, CO, USA
[4]High Altitude Observatory, National Center for Atmospheric Research, Boulder, CO, USA
[5]CIRES, University of Colorado Boulder, Boulder, CO, USA
[6]Department of Earth Sciences, National Cheng Kung University, Tainan, Taiwan

Key Points:

- A merging of the EIA crests leading to an X-shaped pattern is observed in GOLD ionospheric measurements.
- We explain this phenomenon using simulations, which advances our knowledge and is potentially helpful for space weather forecast capability.
- The simulations show that the nighttime EIA-X are generated during pre-sunset and persists after sunset.

Corresponding author: Fazlul I. Laskar, `Fazlul.Laskar@colorado.edu`

Abstract

A unique phenomenon – merging of Equatorial Ionization Anomaly (EIA) crests, leading to an X-pattern (EIA-X) around the magnetic equator – has been observed in the night-time ionospheric measurements by the Global-scale Observations of the Limb and Disk (GOLD) mission. A whole atmospheric general circulation model simulation reproduces this pattern. The pattern is also produced in an assimilative ionosphere model that assimilates slant Total Electron Content (slant-TEC) from Global Navigation Satellite System (GNSS) and Constellation Observing System for Meteorology, Ionosphere, and Climate 2 (COSMIC-2). Due to the observed similarity between measurements and simulations, the latter is used to diagnose this heretofore unexplained phenomenon. The simulation shows that the EIA-X occurs in the afternoon to evening sector at a longitude where the vertical drift is negative, which is a necessary but not sufficient condition. The simulation was performed under constant low-solar and quiescent-geomagnetic forcing conditions, therefore we suggest that one of the drivers of this phenomenon is from lower-atmospheric processes.

Plain Language Summary

Using Global-scale Observations of the Limb and Disk (GOLD) mission observations of the nighttime ionospheric emissions, a new phenomenon of the merging of the Equatorial Ionization Anomaly (EIA) crests forming an X shaped pattern (EIA-X) has been observed around the magnetic equator. This intriguing pattern has been reproduced in a whole atmospheric general circulation model simulation and data assimilation. By examining the electron density and plasma drifts in the model, it has been deduced that the EIA-X consistently coincides with a negative vertical drift, situated between two positive drift regions to the east and west of the crossing location. Generally, it occurs before sunset and is present there until about 21 LT. We propose that the drivers of this phenomenon primarily originate in the lower atmosphere. These significant findings advance our understanding of the afternoon to evening time ionosphere, which hold the potential to improve space weather forecasting and space based radio communication.

1 Introduction

Although the maximum number of ions in the Earth's atmosphere is produced at the sub-solar point in the ionosphere, a combination of the unique geometry of the mag-

netic field lines and electrodynamical coupling generates two bands of enhanced ions and electrons, known as the Equatorial Ionization Anomaly (EIA), on both sides of the geomagnetic equator. The generation and evolution processes of the EIA have been known to the space science community since the dawn of the space age (Appleton, 1946). However, with the evolution of improved sensitivity and innovative observing capabilities of the ionosphere, new and unexpected features of the EIA are being observed, and the mysteries behind them are being unraveled. For instance, the four wave structure in EIA longitudinal variability (Immel et al., 2006; England et al., 2006), global and high cadence observations of the EIA and irregularities in them (Eastes et al., 2020; Huba & Liu, 2020).

Normally, the EIA exhibits two distinct crests forming around the Earth's magnetic equator (Appleton, 1946; Balan et al., 2018; Eastes et al., 2023). However, on certain occasions, it has been reported to display a non-anomalous equatorial ionization situation, characterized by only one peak over or near the magnetic equator (Carruthers & Page, 1972; Basu et al., 2009). The earliest report (Carruthers & Page, 1972) of the merging of EIA crests was presented from the far ultraviolet camera operated on the lunar surface during the Apollo 16 mission. This report, however, was not able to show a clear X-pattern merging of the EIA crests. The later report (Basu et al., 2009) utilized observations from satellites in Low-Earth Orbit (LEO) and documented extremely large-scale features, spanning over 100 degrees in longitude. In contrast, more recent studies have focused on localized merging of the EIA crests over the magnetic equator, combining Global-scale Observations of the Limb and Disk (GOLD) observations with model simulations. The recent studies attribute the merging events to disturbances resulting from either geomagnetic storms (Wu et al., 2023) or Tonga-volcanic eruption (Aa et al., 2022). In this article, we report, several instances of localized EIA X-pattern merging (here onward EIA-X) from the Global-scale Observations of the Limb and Disk (GOLD) nighttime observations. The underlying mechanism responsible for the formation of this phenomenon is thoroughly examined using a combination of model simulation and data assimilation techniques.

The variations in EIA crest intensity and its latitude variation can lead to scintillation and radio wave signal fading for satellite communications, potentially disrupting critical communication and navigation signals (Balan et al., 2018; Kelley, 2009). An understanding of the variability of EIA has implications for space weather monitoring and prediction. A better understanding of the EIA would help towards a better modeling and

forecasting capability of the ionosphere and space weather, which can help mitigate the potential risks posed to satellite communications, navigation systems, and space traffic control.

2 Data and Model Simulation

The primary data used in this investigation are from GOLD, which is onboard a geostationary satellite. To interpret the results, simulations using the Whole Atmosphere Community Climate Model with thermosphere and ionosphere extension (WACCM-X) model are employed. In this case, we utilized a free-running version of WACCM-X that incorporates internally generated lower atmospheric dynamics. Additionally, to check the temporal evolution of the ionosphere in more realistic simulations, a data assimilation system that specifies the ionosphere using slant total electron content (slant-TEC) observations from Global Navigation Satellite System (GNSS) and Constellation Observing System for Meteorology, Ionosphere, and Climate-2 (COSMIC-2). Further details regarding the various data used in this investigation are provided below.

2.1 GOLD OI-135.6 nm Intensities

The GOLD instrument consists of two identical and independent Far UltraViolet (FUV) spectrographs, named as channels A and B. They are slit spectrographs and scans the Earth's disk in the spectral range of 132-162 nm wavelengths. The channel B is mainly used for nighttime observations, whereas channel A is used for both day and night observations. A prominent spectral line in the night spectra comes from the Oxygen-I 135.6 nm emission (OI-135.6). This emission results from the radiative recombination of oxygen ion (O^+) with free electrons (e^-) in the F-region and it is therefore a representative of the F-layer peak plasma density. The nighttime observation starts approximately one hour after local sunset and lasts for 3 to 5 hours, depending on the scheduling of other observing modes and the season. Each observing cycle scans a specific longitudinal range and typically lasts for approximately 15 minutes. As GOLD is stationed in a geostationary orbit over the equator at 47.5°W, the disk observations cover a major portion of the Pacific-American-Atlantic longitude sector on any given night. Further technical details about the GOLD instrument, operation schedules, and nighttime observations can be found in Eastes et al. (2019, 2020); Karan et al. (2020) and in the webpage `https://`

gold.cs.ucf.edu/. The current investigation used Level1C night scanning version 3 data that are marked as "Level 1C NI1" in the GOLD webpage.

2.2 Free-Running WACCM-X

WACCM-X is a whole atmosphere community climate model that couples land, ocean, lower atmosphere models with the thermosphere ionosphere. For this study, we utilized a free-running version where the lower atmospheric variabilities are internally generated by the model. The solar and geomagnetic parameters for this run were maintained at constant values of 70 solar flux unit (sfu, to represent low solar activity conditions) and a Kp-index of 1 (to ensure geomagnetically quiet conditions). The model horizontal resolution is 1.9° (latitude) × 2.5° (longitude), while the vertical resolution spans from 1 to 3 km up to 50 km altitude, and then 0.25 scale heights for altitudes above ∼50 km. The model extends from the surface to 500-700 km, depending on solar activity level (H.-L. Liu et al., 2018). As the model is free-running, it does not correspond to a specific real year. However, the internally generated lower atmospheric dynamics varies day-to-day and it can effectively generate seasonal climatology. More comprehensive insights into the model's physics, dynamics, and additional information can be found in H.-L. Liu et al. (2018).

The main purpose of using WACCM-X is to simulate ionospheric conditions analogous to those observed in the GOLD OI-135.6 nm emissions. Additional ionospheric parameters from instances where comparable characteristics are detected in the simulations and GOLD observations are leveraged to elucidate the latter. We have employed TEC for direct comparisons, in conjunction with vertical drifts ($\mathbf{E}\times\mathbf{B}$ over the magnetic equator) and electron density profiles (as independent parameters) obtained from WACCM-X for more extensive investigations.

2.3 Global Ionospheric Specification (GIS)

GIS is a global ionospheric data assimilation that ingest the slant-TEC from ground based GNSS receivers and space-based radio occultation measurements from COSMIC-2 mission. The GIS updates the forecast at every hour by using the COSMIC-2 and GNSS observations. It has a latitude×longitude resolution of 5° × 2.5°, and vertical resolution of 20 km in the 120-700 km altitudes. It uses Gauss-Markov Kalman filter with Inter-

national Reference Ionosphere (Bilitza et al., 2022) as the background model. The GIS global ionospheric data are used in several studies on ionospheric dynamical variabilities (Lin et al., 2020; Rajesh et al., 2021; Oberheide, 2022). Further details on the GIS assimilation can be found in Lin et al. (2017). The GIS data, for a day when EIA-X is observed, are used here to see the time evolution. This assists in the interpretation of the GOLD observations.

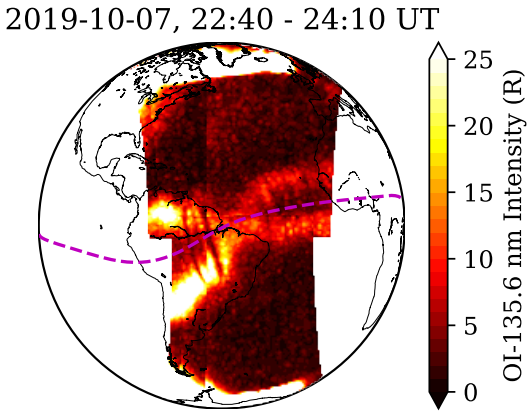

Figure 1. GOLD nighttime disk observations of the post-sunset OI-135.6 nm airglow showing X-pattern merging of EIA. The dashed line marks the geo-locations of the geomagnetic equator. The EIA crests crossing is centered over the Atlantic Ocean to the east of South America.

3 Results

Figure 1 reports a representative example of the crossing of EIA crests as observed by GOLD. For simplicity, here onward, we refer the crossing as EIA-X as it looks like a cross sign. The image in Figure 1 combines three (skipping another three in between) individual 15-minute scans made by each channel during 22:40 UT on 7 October 2019 to 00:10 UT on 8 October 2019. Although the total duration is one hour and 30 minutes, the majority of the EIA-X is visible in both first (22:40 - 23:10 UT) and last (23:40 - 23:10 UT) 30-minutes, but with lesser longitude coverage. The later UT scans are partly combined at the western sides in Figure 1 to show better longitude coverage. The local time (LT) at the sub-satellite location is approximately 20:30 hr, while at extreme eastern and western longitudes, it is about 21:30 and 19:00 hrs., respectively. Consequently, in this case, the EIA-X is observed at around 20:30 LT over 45°W longitude. The west-

ern part of the EIA-X is closer to the sunset and therefore brighter compared to the eastern part.

Other cases of EIA-X have also been observed by GOLD, some of which are provided in the supporting information Figure S1. These occurrences are registered at locations both east and west of the one presented in Figure 1. Furthermore, there are cases which exhibit the EIA-X over the Atlantic ocean with varying shapes. In most instances, these features are observed during geomagnetically quiet times (Kp<=2), which is a unique finding as the earlier reports (Aa et al., 2022; Wu et al., 2023) were during disturbed conditions. Therefore, our investigation reports, for the first time, EIA-X during quiet geomagnetic conditions. Additionally, there are indications of merging of EIA crests over the Pacific in GOLD post-midnight observations (see examples in Laskar et al. (2020)). A comprehensive analysis of the local time, seasonal, and solar activity dependence of this pattern requires further investigations involving a larger number of cases.

For the case shown in Figure 1, we observed the EIA-X for approximately 2 hrs without any significant eastward or westward movement. It is plausible that the feature may persist even longer. GOLD is the only instrument capable of routinely measuring ionospheric emissions over a wide range of longitudes, enabling it to observe this phenomenon repeatedly. Ground-based global navigation satellite system measurements, which are constrained by their availability only over the continental landmass, are not able to capture this phenomenon as unambiguously or as frequently.

To further investigate the phenomenon and determine its underlying causes, we employed free-running WACCM-X simulations that are driven with constant low-solar and quiescent geomagnetic conditions. Ideally, we should use a specified dynamics (SD) version of WACCM-X to compare the same day with GOLD observations. But currently available SD-WACCMX capability did not reproduce the EIA-X on the days when they are observed in GOLD observations. However, since the OI-135.6 nm emissions are almost directly proportional to the square of the electron number density, a comparison with TEC from free-run WACCM-X could offer valuable insights for the model's further applicability. Figure 2 reports two representative days of Electron Column Density (ECD, a quantity similar to TEC but integrated to the model upper boundary, in a-b) and vertical drift (in c-d) data from WACCM-X. There are numerous other examples (not shown here), where we have observed similar EIA-X in WACCM-X ECD data. The local times

at the location of the EIA-X crossing are approximately 18 hr (for 3 Jan.) and 19 hr (for 19 Sep.). On both days, the EIA-X first appears before sunset and persists until about 20 LT, without any noticeable longitudinal movement. After 20 LT, the electron number densities at the crossing location decay rapidly, creating a longitudinal discontinuity (Laskar et al., 2020; Cai et al., 2023), while the eastern part (later local time compared to X-location) persist till post-midnight, to appear as an early morning EIA (Laskar et al., 2020). As the EIA responds to E-region drifts with a delay of at least an hour (Stolle et al., 2008), the vertical drifts shown here are from one hour before the ECD time. In Figure 2, there are two regions of negative vertical drifts: One in the evening sector near the EIA-X (left side, marked with vertical dashed line) and the other is the typical nighttime downward drifts (right side). The evening sector negative drift that coincides with the crossing longitude of the EIA-X, marked with vertical dashed line, is of interest here.

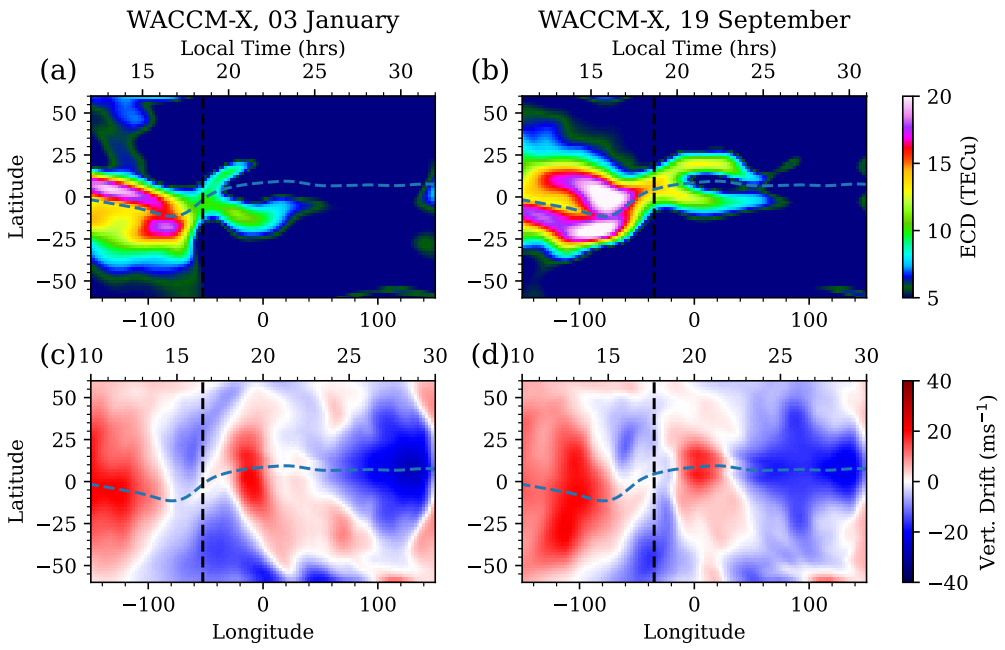

Figure 2. Two examples of EIA-X in WACCM-X electron column density (ECD) are shown along with E-region vertical drifts. On 3 January and 19 September the pattern occurred in between 17 to 20 LT. The vertical dashed lines at 52.5°W and 37.5°W mark the locations around which the X crossings are observed for 3 January and 19 September, respectively. The vertical drifts shown are from one hour before the ECD, therefore they have a different local time scale.

We analyzed one year of free running WACCM-X data and observed that X-pattern mostly occurred between pre-sunset and midnight. The pattern is not very frequent and its occurrence does not have any preferential longitude or season dependence. It is important to note that in our simulations a negative (or very small) drift is a necessary but not a sufficient condition for the occurrence of the EIA-X, as there are many cases where negative drifts (even lower than -20 m/s) are observed in the afternoon or evening sector without any collocated EIA-X, but there is no EIA-X in the absence of negative (or very small) drift. In general, the negative drifts are more pronounced one hour before the occurrence of the EIA-X compared to that same hour. This is because the plasma in the EIA crests responds to electric field changes after 1 to 2 hrs (e.g, Stolle et al., 2008). As WACCM-X simulations can have more temporal and spatial coverages compared to GOLD, we conducted further investigations on the local time variabilities of the vertical drift, utilizing the WACCM-X states.

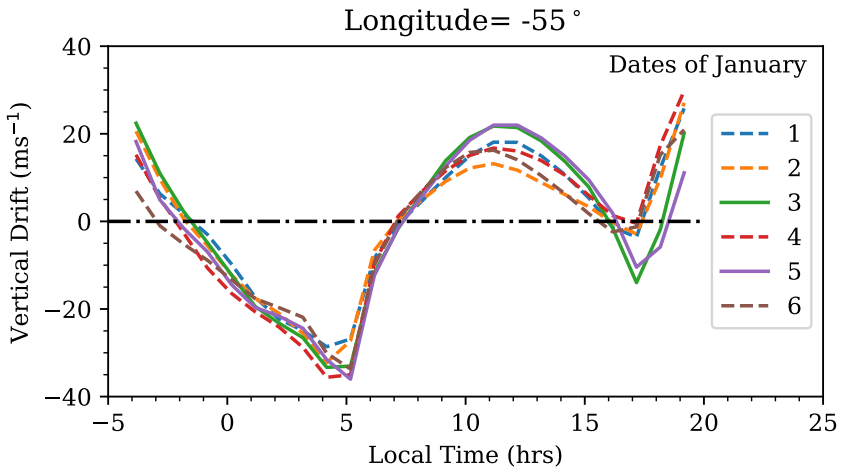

Figure 3. Ionospheric vertical drift for 6 days of January is shown. Out of these 6 days, EIA-X occurred at 55.0°±2.5° W on days 3 and 5 (marked by the solid lines). Note the presence of negative drift around the sunset (or pre-PRE) times, when we see the EIA-X. Also, notable is that on the EIA-X days PRE starts about 2 hrs later than the other days.

The local time variation of the WACCM-X vertical drift, at approximately 160 km over the location of the crossing, for six representative days is shown in Figure 3. Note that the WACCM-X vertical drifts are very similar in the altitudes above 100 km, so only a single altitude is considered from that range. As mentioned above, these are $\mathbf{E}\times\mathbf{B}$ drifts that comes from dynamo action at E-region altitudes. Generally, for this longitude and

season the drift is negative (downward) during pre-midnight to early morning and is positive during daytime and Pre-Reversal Enhancement (PRE) intervals (e.g,. Farley et al., 1986; Fejer et al., 1991; Eccles et al., 2015). Notably, there are distinct negative drifts during 16-19 LT on days 3 and 5, illustrated as solid lines. These are the two days where EIA-X is observed in WACCM-X ECD (or TEC). Furthermore, on these two days the early evening negative drifts stayed negative for longer duration, and the occurrence of PRE is delayed. Similar scenarios are also observed for the 19 September and other cases (not shown here). As a result, the ionosphere around sunset experiences a deviation from the typical behavior, as it is not being uplifted as usual. Instead, the negative drifts facilitate a faster recombination of the ionosphere by moving the plasma to lower altitudes.

As WACCM-X provides a three-dimensional structure of the ionosphere, we can analyze electron density profiles. Figure 4 shows an example from the 19 September event, in which we see a single crest that is already developed at 16.5 LT and stays there until 19.5 LT, i.e., it lasted for about 4 hrs. From the next hour (20.5 LT) the usual EIA with two crests starts to develop again (not shown here). The dashed-curves indicate approximate locations of geomagnetic field lines as per Richmond (1995) calculations, with international geomagnetic reference field 13^{th} generation coefficients (Alken et al., 2021). Similar plots for the 3 January case is shown in supporting information figure S2, which shows some similarity with Figure 4, but not identical. This shows that the negative vertical drift hinders development of the plasma fountain effect and leads to a single peak.

Though the electron densities in Figure 4 appears as a single peak in the altitude vs. latitude slices, when we view the latitudes and longitudes from above (integrated in altitude) it appears as a merging of the crests, forming an X-pattern, as seen in Figure 2. There are several parameters that can impact the shape of the EIA crests. A strong latitudinal or altitudinal gradient in the winds and drifts could play an important role in the movement of the plasma in the east-west direction (Heelis, 2004; McDonald et al., 2008; Rodrigues et al., 2012; Richmond & Fang, 2015; Khadka et al., 2018; Chen & Lei, 2019; Yamazaki et al., 2021). The aforementioned studies have shown that the temporal and spatial variation of zonal wind, meridional wind, and plasma drifts could impact the EIA morphology. In this study, we have analyzed all these parameters from WACCM-X for at least 10 different cases of EIA-X and found that the vertical drift is the only parameter that shows a consistent and unique behavior. It is negative during 1 to 2 hrs before the EIA-X occurrence, as shown in Figures 2 and 3. None of the other parame-

ters show any consistent behavior. This could be due to the non-linear nature of the dynamics at E- and F-region altitudes, particularly around sunset. Further investigations using electrodynamical calculation are needed to find out the exact mechanism that leads to the negative drift.

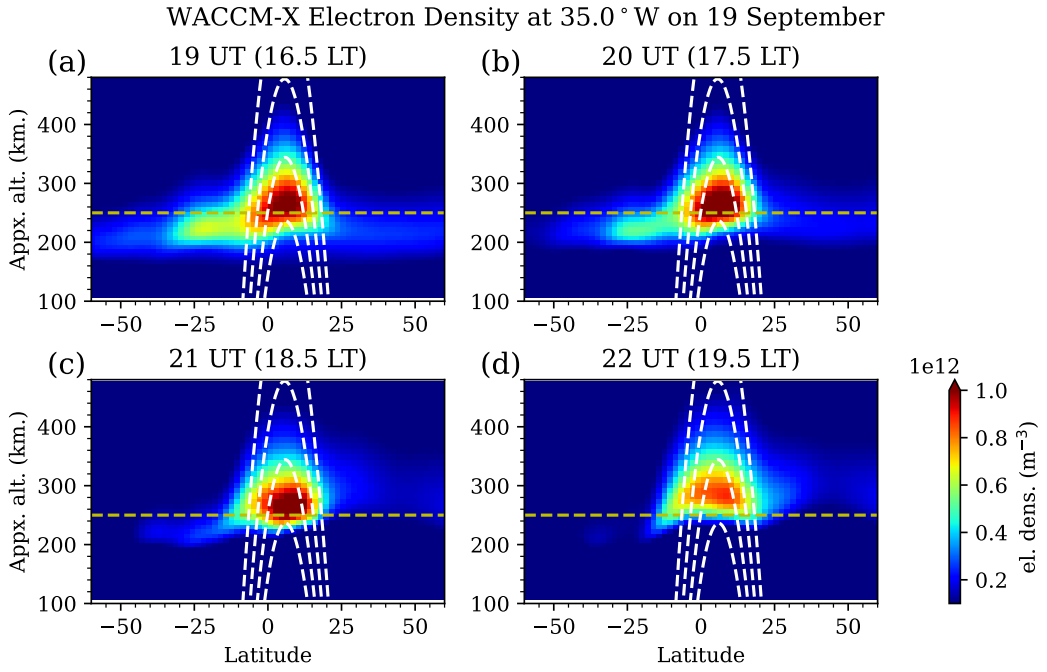

Figure 4. WACCMX electron number density at 35.0° W, where the X crossing is observed between 19 and 22 UT. At about 16.5 LT the EIA merges into a single peak over the equator and stays there until 19.5 LT. The horizontal dashed line marks the 250 km altitude.

As presented above, we have observed the time evolution of the EIA-X in a free-running WACCM-X simulation, which shows that it develops during the pre-sunset hours and persists for several hours after sunset. However, it remains uncertain whether the real ionosphere behaves similar to what has been observed in the model simulation. To address this question, continuous ionospheric observations over the Atlantic Ocean are needed, particularly in the region where we have previously observed the EIA-X. Unfortunately, such observations are not always available from ground-based GNSS receivers, nor are they as comprehensive from COSMIC-2 observations.

Nevertheless, we can gain valuable insights by combining the GNSS and COSMIC-2 measurements through data assimilation. For this, we utilized ionospheric TEC data from GIS data assimilation system, which is described in the data section. Figure 5 re-

ports the GIS TEC for the day when EIA-X was observed by GOLD, as shown above in Figure 1. In Figure 5, the EIA-X forms at 20 UT (17 LT) with a merging at the same location as in the GOLD data. The crossing location is marked with black dashed lines. The west part of the crossing does not show a good agreement with either GOLD or GNSS-TEC (not shown here). As the assimilation models and methods are being constantly improved this type of discrepancies are inevitable. But the partial good agreement in the location of the EIA-X between GOLD and GIS motivates us to use GIS to study the time evolution. The X-crossing in GIS starts to develop at 20 UT (∼17 LT) and stays there beyond 24 UT (21 LT), when it was also seen in GOLD observations for 2 hrs. This provides evidence that the EIA-X develops before sunset, as is also observed in the WACCM-X data, and persists until post sunset. As such, it is very likely that the post-sunset EIA-X observed by GOLD was formed in the hours preceding sunset.

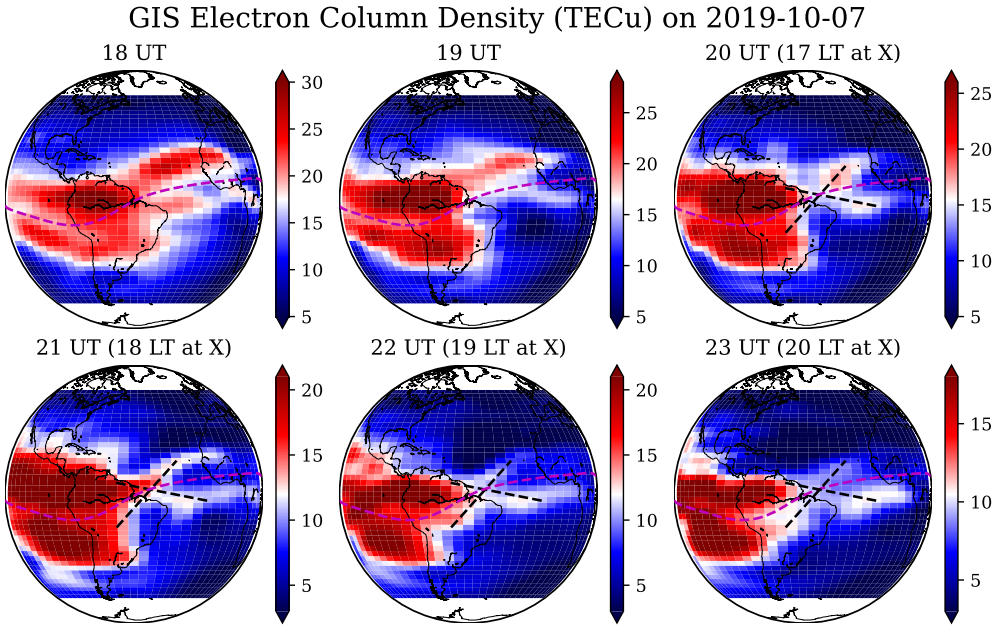

Figure 5. Global Ionospheric Specification (GIS) ionospheric electron content maps are shown for the day in Figure 1. This shows that the EIA-X (marked with dashed X) is starting to develop from 20 UT. It does not generate the exact EIA-X as we see in GOLD but does show the development of the merged location exactly where we have seen it in GOLD.

4 Discussion

Though global TEC measurements are available for decades, they are limited by longitude coverage to unambiguously display the full EIA-X in TEC maps. Observations of the large-scale merging of the EIA crests were reported earlier (e.g., Basu et al., 2009), where the EIA merging extends from 60 to 90 degrees in longitude. But the merging observed by the GOLD is much more limited to a narrow, ∼10 degrees, longitude – see, e.g., Figure 1. This makes our observation from GOLD a unique case, particularly during geomagnetically quiescent times. Signatures of potential EIA-X are observed in the night-side of the full disk images from GOLD, some examples can be seen in Figure 1 of Laskar et al. (2020). This feature was not completely and unambiguously observed before the GOLD mission, due to the lack of simultaneous availability of wide spatial and temporal measurements. GOLD is in a geostationary orbit, and it can scan a major part of the disk in about 12 minutes. This unique capability of GOLD made it possible to observe this phenomenon repeatedly.

Earlier investigation also used GOLD observations and reported the merging of EIA crests during geomagnetic storm (Wu et al., 2023) and Tonga volcanic eruption (Aa et al., 2022). Our investigation, however, demonstrates that they are not the only processes responsible for the generation of this phenomenon. Disturbances in equatorial ionospheric electric fields could potentially generate an EIA-X even during non-disturbed times, as we have observed in GOLD and WACCM-X results. Since the WACCM-X simulations were conducted under constant low-solar and quiescent geomagnetic conditions, one of the drivers behind this unexplained phenomenon apparently originates in the lower atmosphere. However, its sporadic occurrence and non-association with any systematic changes in wind suggest that there is a complex underlying process, which is modulated by lower atmospheric waves, that drives the negative drift and the consequent evolution of EIA-X.

The occurrence of the EIA-X with a negative vertical drift sandwiched between two positive drift regions that extends over all the latitudes suggests that large scale dynamical processes are instrumental in shaping this phenomenon. We suspect that lower atmospheric large scale waves (e.g., tides and planetary waves) and their interaction with mean flow play the leading role (England et al., 2006; Soares et al., 2019; Triplett et al., 2019; Krier et al., 2021; Lühr et al., 2021; Maute, 2021; Yizengaw, 2021; G. Liu et al.,

2022). However, further investigations are needed to find the mechanism through which the lower thermospheric electrodynamics is modulated, which trigger the longitudinally localized merging of the EIA crests. Understanding the dynamics involved will not only enhance our knowledge of the ionosphere's response to external drivers but also contribute to improving space-based communications.

5 Summary and Conclusions

The merging of the EIA crests creating X-pattern (EIA-X) has been observed by GOLD on numerous occasions during geomagnetically quiet periods. This phenomenon has also been observed in the WACCM-X simulation and in global ionospheric data assimilation. The observed variabilities in both the measurements and simulations lead to the following conclusions:

1. GOLD nighttime observations showed that the EIA-X occurs over American longitudes and mostly in the post-sunset to midnight sector.
2. Model simulations show that the EIA-X can occur at any longitude and mostly in the pre-sunset to midnight sector. It is preceded and/or accompanied by a negative or close-to-zero vertical drift. The negative vertical drift is a necessary but not sufficient condition for the EIA-X occurrence.
3. Except the vertical drift, none of the other parameters from WACCM-X showed a consistent behavior during EIA-X times.
4. While geomagnetic storms can induce the EIA-X formation, it is also observed during quiescent geomagnetic conditions, suggesting that it can also be driven by lower atmospheric processes.
5. Ionospheric data assimilation supports the WACCM-X results and shows evidence that the EIA-X develops before sunset and stays there until about 21 LT.

The investigation into the specific lower atmospheric processes driving the E-region dynamo, which subsequently leads to negative vertical drift and the X-pattern merging of the EIA crests, needs to be further explored using nudged model simulations and the thermosphere-ionosphere data assimilation. A comprehensive understanding of the dynamics during the pre- to post-sunset period will not only advance our knowledge of the ionosphere's response to external (lower atmospheric or geomagnetic) drivers but also plays a crucial role in the development of space weather forecasting capability.

6 Open Research

GOLD Level 1C NI-1 data used in this study are available at the GOLD Science Data Center (`https://gold.cs.ucf.edu/search/`) and at NASA's Space Physics Data Facility (`https://spdf.gsfc.nasa.gov/pub/data/gold/level1c/`). The GIS data are available at `http://formosat7.earth.ncku.edu.tw/login.php?Where=download.php`. Electron column density and vertical drift data used in this publication can be found in `https://doi.org/10.5281/zenodo.10035354`.

Acknowledgments

This research was supported by NASA Contract 80GSFC18C0061 to the University of Colorado, Boulder. This material is also based upon work supported by the National Center for Atmospheric Research (NCAR), which is a major facility sponsored by the National Science Foundation under Cooperative Agreement No. 1852977.

References

Aa, E., Zhang, S.-R., Wang, W., Erickson, P. J., Qian, L., Eastes, R., ... Spicher, A. (2022, June). Pronounced suppression and x-pattern merging of equatorial ionization anomalies after the 2022 tonga volcano eruption. *Journal of Geophysical Research: Space Physics*, *127*(6). doi: 10.1029/2022ja030527

Alken, P., Thébault, E., Beggan, C. D., Amit, H., Aubert, J., Baerenzung, J., ... Zhou, B. (2021, February). International geomagnetic reference field: the thirteenth generation. *Earth, Planets and Space*, *73*(1). doi: 10.1186/s40623-020-01288-x

Appleton, E. V. (1946, May). Two anomalies in the ionosphere. *Nature*, *157*(3995), 691–691. doi: 10.1038/157691a0

Balan, N., Liu, L., & Le, H. (2018). A brief review of equatorial ionization anomaly and ionospheric irregularities. *Earth and Planetary Physics*, *2*(4), 1–19. doi: 10.26464/epp2018025

Basu, S., Basu, S., Huba, J., Krall, J., McDonald, S. E., Makela, J. J., ... Groves, K. (2009, April). Day-to-day variability of the equatorial ionization anomaly and scintillations at dusk observed by GUVI and modeling by SAMI3. *Journal of Geophysical Research: Space Physics*, *114*(A4). doi: 10.1029/2008ja013899

Bilitza, D., Pezzopane, M., Truhlik, V., Altadill, D., Reinisch, B. W., & Pignalberi,

A. (2022, October). The international reference ionosphere model: A review and description of an ionospheric benchmark. *Reviews of Geophysics*, *60*(4). doi: 10.1029/2022rg000792

Cai, X., Wang, W., Eastes, R. W., Qian, L., Pedatella, N., Aa, E., ... McClintock, W. E. (2023, May). Equatorial ionization anomaly discontinuity observed by GOLD, COSMIC-2, and ground-based GPS receivers' network. *Geophysical Research Letters*, *50*(10). doi: 10.1029/2023gl102994

Carruthers, G. R., & Page, T. (1972, September). Apollo 16 far-ultraviolet camera/spectrograph: Earth observations. *Science*, *177*(4051), 788–791. doi: 10.1126/science.177.4051.788

Chen, J., & Lei, J. (2019, February). A simulation study on the latitudinal variations of ionospheric zonal electric fields under geomagnetically quiet conditions. *Journal of Geophysical Research: Space Physics*, *124*(2), 1444–1453. doi: 10.1029/2018ja026174

Eastes, R. W., Karan, D. K., Martinis, C., Daniell, R. E., Gan, Q., Burns, A. G., & McClintock, W. E. (2023, April). GOLD observations of longitudinal variations in the nighttime equatorial ionization anomaly (EIA) crests' latitudes. *Journal of Geophysical Research: Space Physics*, *128*(4). doi: 10.1029/2022ja031007

Eastes, R. W., McClintock, W. E., Burns, A. G., Anderson, D. N., Andersson, L., Aryal, S., ... Woods, T. N. (2020, June). Initial observations by the GOLD mission. *Journal of Geophysical Research: Space Physics*, *125*(7). doi: 10.1029/2020ja027823

Eastes, R. W., Solomon, S. C., Daniell, R. E., Anderson, D. N., Burns, A. G., England, S. L., ... McClintock, W. E. (2019, August). Global-scale observations of the equatorial ionization anomaly. *Geophysical Research Letters*, *46*(16), 9318–9326. doi: 10.1029/2019gl084199

Eccles, J. V., Maurice, J. P. S., & Schunk, R. W. (2015, June). Mechanisms underlying the prereversal enhancement of the vertical plasma drift in the low-latitude ionosphere. *Journal of Geophysical Research: Space Physics*, *120*(6), 4950–4970. doi: 10.1002/2014ja020664

England, S. L., Maus, S., Immel, T. J., & Mende, S. B. (2006, November). Longitudinal variation of the e-region electric fields caused by atmospheric tides. *Geophysical Research Letters*, *33*(21). doi: 10.1029/2006gl027465

Farley, D. T., Bonelli, E., Fejer, B. G., & Larsen, M. F. (1986). The prereversal enhancement of the zonal electric field in the equatorial ionosphere. *Journal of Geophysical Research*, *91*(A12), 13723. doi: 10.1029/ja091ia12p13723

Fejer, B. G., de Paula, E. R., González, S. A., & Woodman, R. F. (1991, August). Average vertical and zonal f region plasma drifts over jicamarca. *Journal of Geophysical Research: Space Physics*, *96*(A8), 13901–13906. doi: 10.1029/91ja01171

Heelis, R. (2004, July). Electrodynamics in the low and middle latitude ionosphere: a tutorial. *Journal of Atmospheric and Solar-Terrestrial Physics*, *66*(10), 825–838. doi: 10.1016/j.jastp.2004.01.034

Huba, J. D., & Liu, H.-L. (2020, July). Global modeling of equatorial spread F with SAMI3/WACCM-x. *Geophysical Research Letters*, *47*(14). doi: 10.1029/2020gl088258

Immel, T. J., Sagawa, E., England, S. L., Henderson, S. B., Hagan, M. E., Mende, S. B., ... Paxton, L. J. (2006). Control of equatorial ionospheric morphology by atmospheric tides. *Geophysical Research Letters*, *33*(15). doi: 10.1029/2006gl026161

Karan, D. K., Daniell, R. E., England, S. L., Martinis, C. R., Eastes, R. W., Burns, A. G., & McClintock, W. E. (2020, September). First zonal drift velocity measurement of equatorial plasma bubbles (EPBs) from a geostationary orbit using GOLD data. *Journal of Geophysical Research: Space Physics*, *125*(9). doi: 10.1029/2020ja028173

Kelley, M. (2009). *The earth's ionosphere: Plasma physics and electrodynamics*. Elsevier Science. doi: 10.1016/b978-0-12-404013-7.x5001-1

Khadka, S. M., Valladares, C. E., Sheehan, R., & Gerrard, A. J. (2018, May). Effects of electric field and neutral wind on the asymmetry of equatorial ionization anomaly. *Radio Science*, *53*(5), 683–697. doi: 10.1029/2017rs006428

Krier, C. S., England, S. L., Greer, K. R., Evans, J. S., Burns, A. G., & Eastes, R. W. (2021, September). Deducing non-migrating diurnal tides in the middle thermosphere with GOLD observations of the earth's far ultraviolet dayglow from geostationary orbit. *Journal of Geophysical Research: Space Physics*, *126*(10). doi: 10.1029/2021ja029563

Laskar, F. I., Eastes, R. W., Martinis, C. R., Daniell, R. E., Pedatella, N. M., Burns,

A. G., ... Codrescu, M. V. (2020, July). Early morning equatorial ionization anomaly from GOLD observations. *Journal of Geophysical Research: Space Physics*, *125*(7). doi: 10.1029/2019ja027487

Lin, C.-Y., Lin, C. C.-H., Liu, J.-Y., Rajesh, P. K., Matsuo, T., Chou, M.-Y., ... Yeh, W.-H. (2020, October). The early results and validation of FORMOSAT-7/COSMIC-2 space weather products: Global ionospheric specification and ne-aided abel electron density profile. *Journal of Geophysical Research: Space Physics*, *125*(10). doi: 10.1029/2020ja028028

Lin, C. Y., Matsuo, T., Liu, J. Y., Lin, C. H., Huba, J. D., Tsai, H. F., & Chen, C. Y. (2017, October). Data assimilation of ground-based GPS and radio occultation total electron content for global ionospheric specification. *Journal of Geophysical Research: Space Physics*, *122*(10). doi: 10.1002/2017ja024185

Liu, G., Janches, D., Ma, J., Lieberman, R. S., Stober, G., Moffat-Griffin, T., ... Murphy, D. J. (2022, March). Mesosphere and lower thermosphere winds and tidal variations during the 2019 antarctic sudden stratospheric warming. *Journal of Geophysical Research: Space Physics*, *127*(3). doi: 10.1029/2021ja030177

Liu, H.-L., Bardeen, C. G., Foster, B. T., Lauritzen, P., Liu, J., Lu, G., ... Wang, W. (2018, February). Development and validation of the whole atmosphere community climate model with thermosphere and ionosphere extension (WACCM-X 2.0). *Journal of Advances in Modeling Earth Systems*, *10*(2), 381–402. doi: 10.1002/2017ms001232

Lühr, H., Zhou, Y.-L., & Alken, P. (2021, May). Short-term variability of equatorial electrojet modulation by solar tidal and planetary waves, as derived from the swarm constellation. *Journal of Geophysical Research: Space Physics*, *126*(5). doi: 10.1029/2020ja028884

Maute, A. (2021, March). *The middle- and low-latitude neutral wind dynamo.* Wiley. doi: 10.1002/9781119815631.ch5

McDonald, S. E., Dymond, K. F., & Summers, M. E. (2008, August). Hemispheric asymmetries in the longitudinal structure of the low-latitude nighttime ionosphere. *Journal of Geophysical Research: Space Physics*, *113*(A8), n/a–n/a. doi: 10.1029/2007ja012876

Oberheide, J. (2022, September). Day-to-day variability of the semidiurnal tide

in the f-region ionosphere during the january 2021 SSW from COSMIC-2 and ICON. *Geophysical Research Letters*, *49*(17). doi: 10.1029/2022gl100369

Rajesh, P. K., Lin, C. C. H., Lin, J.-T., Lin, C.-Y., Yue, J., Matsuo, T., ... Chen, C.-H. (2021). Day-to-day variability of ionosphere electron density during solar minimum derived from FORMOSAT-7/COSMIC-2 measurements. *Terrestrial, Atmospheric and Oceanic Sciences*, *32*(6.1). doi: 10.3319/tao.2021.08.01.01

Richmond, A. D. (1995). Ionospheric electrodynamics using magnetic apex coordinates. *Journal of geomagnetism and geoelectricity*, *47*(2), 191–212. doi: 10.5636/jgg.47.191

Richmond, A. D., & Fang, T.-W. (2015, March). Electrodynamics of the equatorial evening ionosphere: 2. conductivity influences on convection, current, and electrodynamic energy flow. *Journal of Geophysical Research: Space Physics*, *120*(3), 2133–2147. doi: 10.1002/2014ja020935

Rodrigues, F. S., Crowley, G., Heelis, R. A., Maute, A., & Reynolds, A. (2012, May). On TIE-GCM simulation of the evening equatorial plasma vortex. *Journal of Geophysical Research: Space Physics*, *117*(A5), n/a–n/a. doi: 10.1029/2011ja017369

Soares, G., Yamazaki, Y., Matzka, J., Pinheiro, K., Stolle, C., Alken, P., ... Kulkarni, A. (2019, April). Longitudinal variability of the equatorial counter electrojet during the solar cycle 24. *Studia Geophysica et Geodaetica*, *63*(2), 304–319. doi: 10.1007/s11200-018-0286-0

Stolle, C., Manoj, C., Lühr, H., Maus, S., & Alken, P. (2008, September). Estimating the daytime equatorial ionization anomaly strength from electric field proxies. *Journal of Geophysical Research: Space Physics*, *113*(A9), n/a–n/a. doi: 10.1029/2007ja012781

Triplett, C. C., Immel, T. J., Wu, Y.-J., & Cullens, C. (2019, November). Variations in the ionosphere-thermosphere system from tides, ultra-fast kelvin waves, and their interactions. *Advances in Space Research*, *64*(10), 1841–1853. doi: 10.1016/j.asr.2019.08.015

Wu, K., Qian, L., Wang, W., Cai, X., & Mclnerney, J. M. (2023, June). Investigation of the GOLD observed merged nighttime EIA with WACCM-x simulations during the storm of 3 and 4 november 2021. *Geophysical Research Letters*, *50*(13). doi: 10.1029/2023gl103603

Yamazaki, Y., Harding, B. J., Stolle, C., & Matzka, J. (2021, June). Neutral wind profiles during periods of eastward and westward equatorial electrojet. *Geophysical Research Letters*, *48*(11). doi: 10.1029/2021gl093567

Yizengaw, E. (2021, March). *Ionospheric dynamics and their strong longitudinal dependences.* Wiley. doi: 10.1002/9781119815617.ch17

Figure 1.

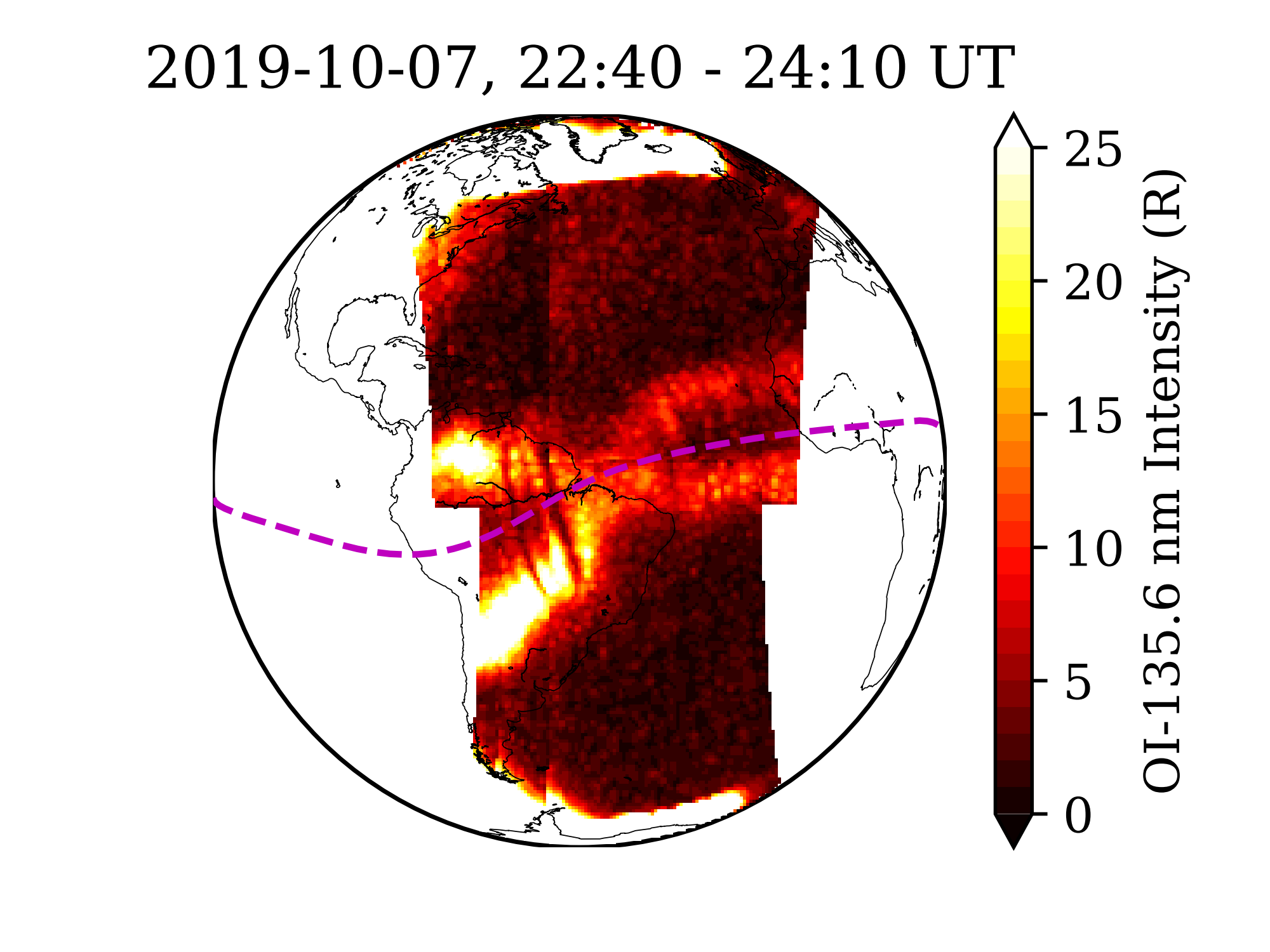
2019-10-07, 22:40 - 24:10 UT
25
20
15
10
5
0
OI-135.6 nm Intensity (R)

Figure 2.

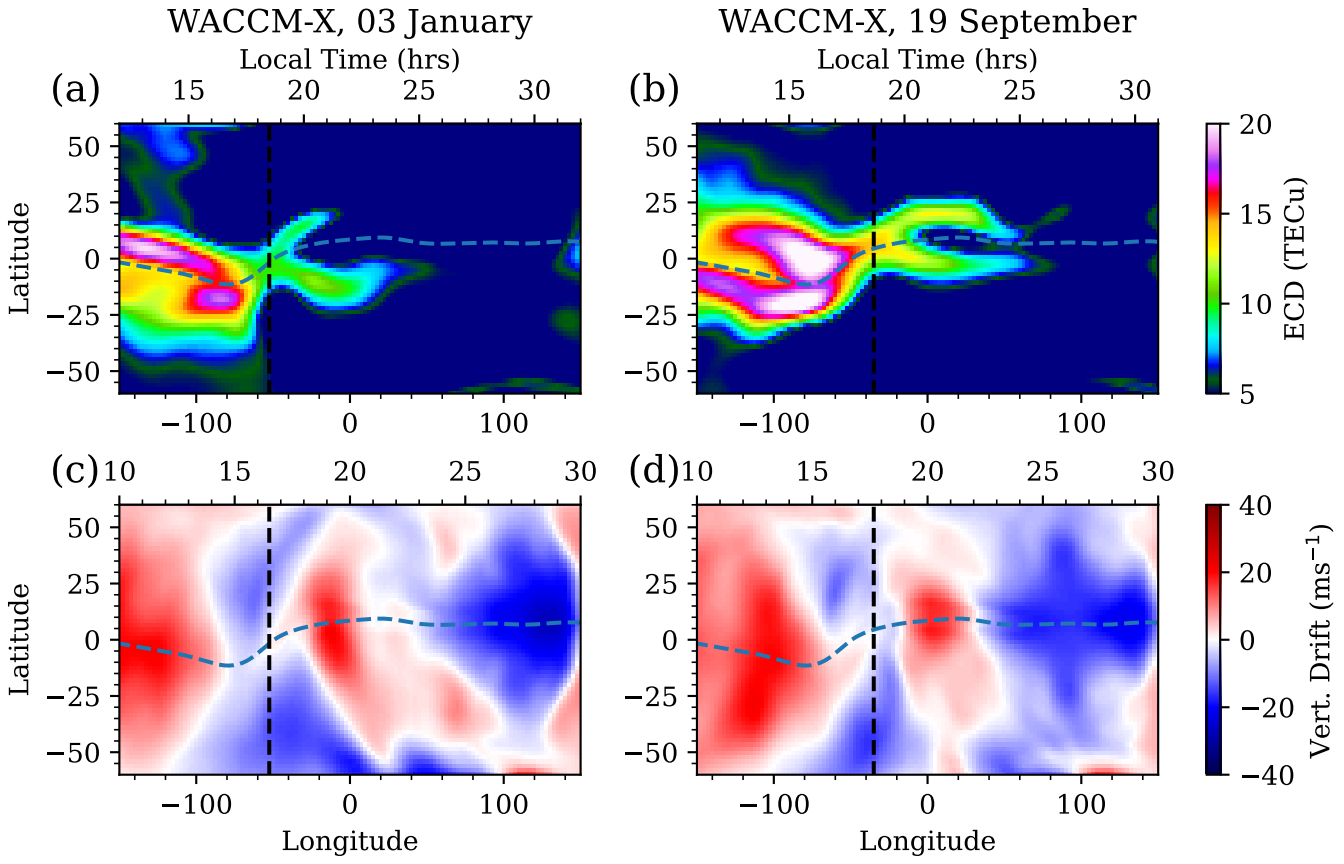
WACCM-X, 03 January
WACCM-X, 19 September
Local Time (hrs)
Local Time (hrs)
(a)
(b)
(c)
(d)
Latitude
Latitude
Longitude
Longitude
ECD (TECu)
Vert. Drift (ms^{-1})

Figure 3.

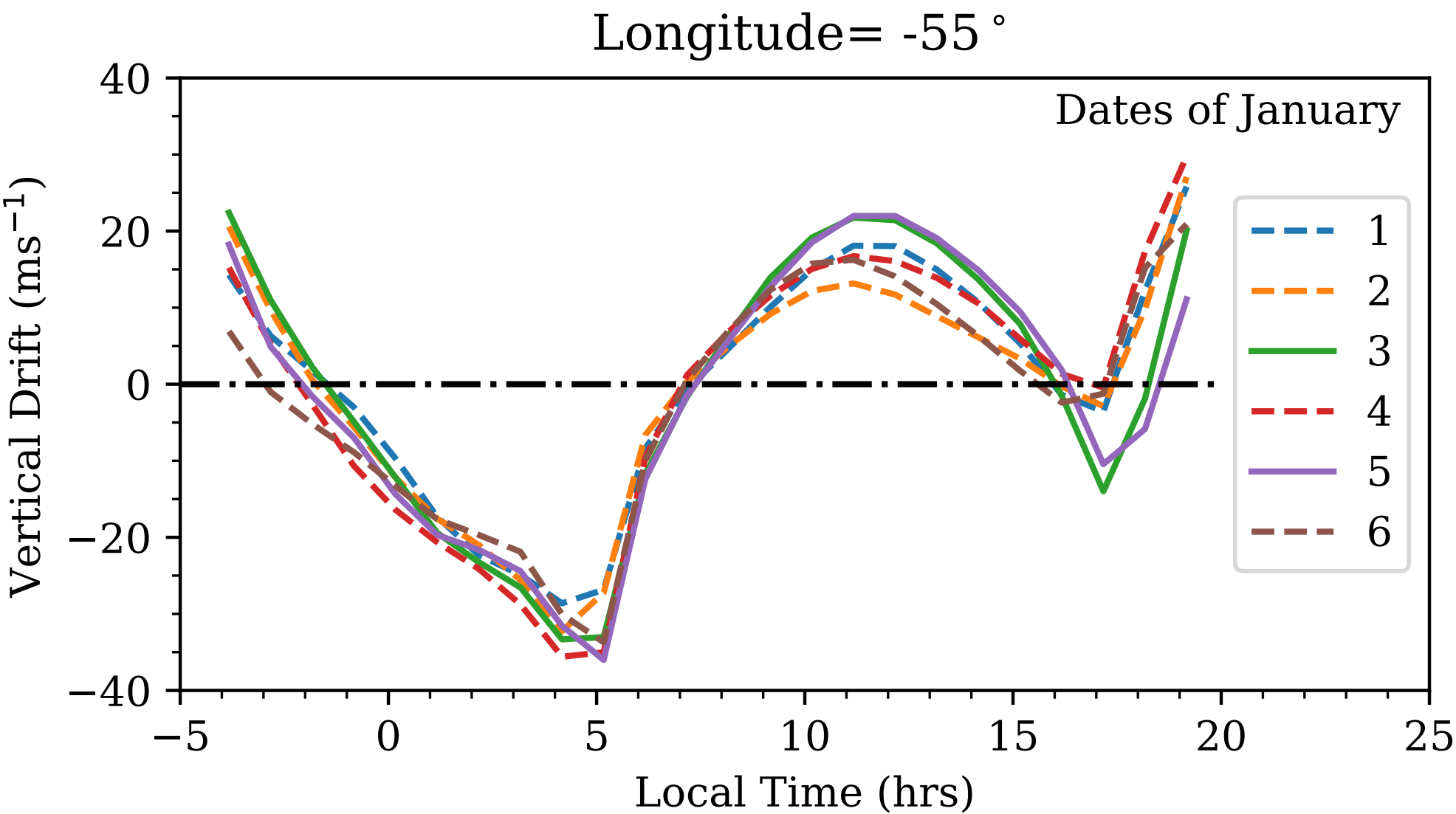
Longitude= -55 °
Dates of January
1
2
3
4
5
6
Vertical Drift (ms^{-1})
Local Time (hrs)
40
20
0
−20
−40
−5
0
5
10
15
20
25

Figure 4.

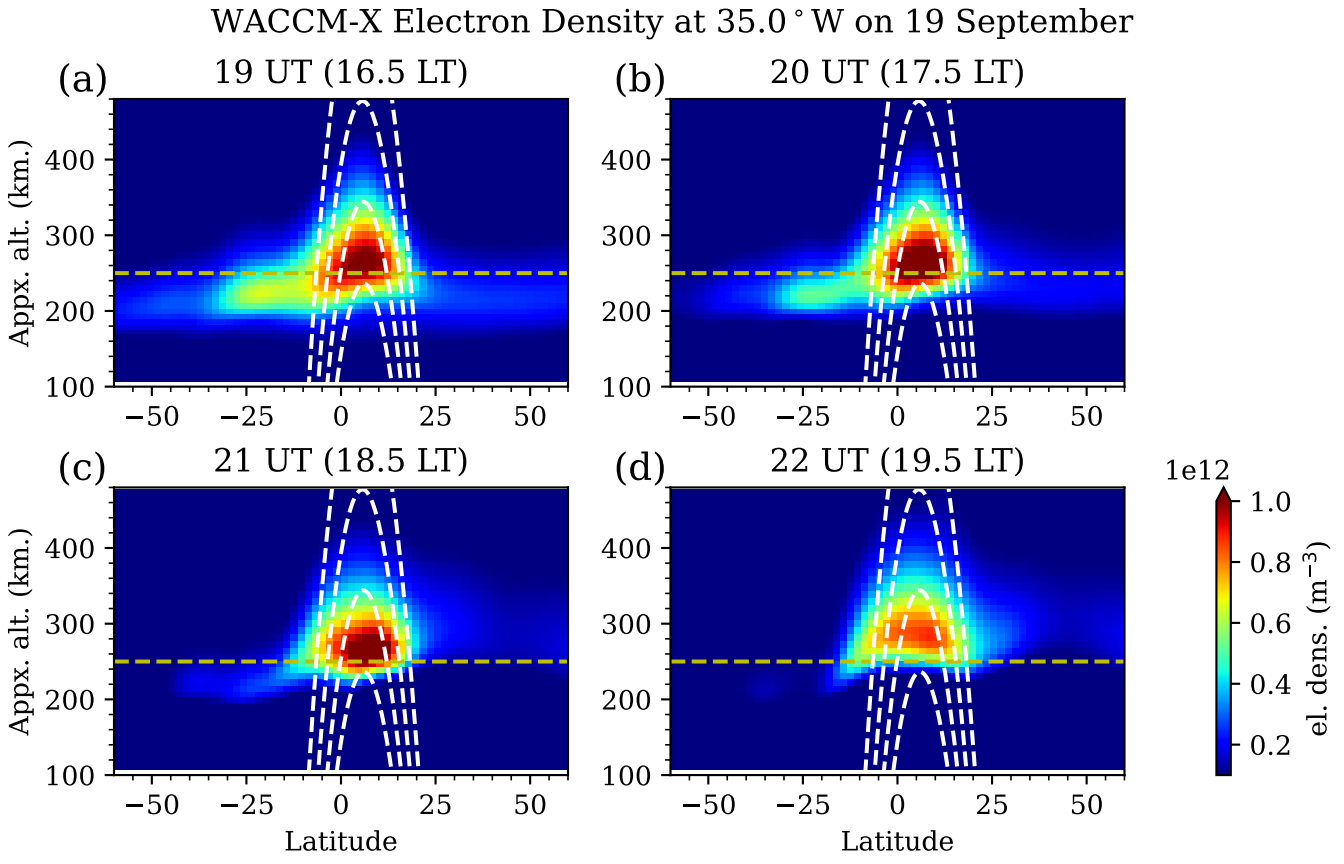
WACCM-X Electron Density at 35.0 ° W on 19 September
(a)
19 UT (16.5 LT)
(b)
20 UT (17.5 LT)
(c)
21 UT (18.5 LT)
(d)
22 UT (19.5 LT)
Appx. alt. (km.)
100
200
300
400
−50
−25
0
25
50
Latitude
1e12
1.0
0.8
0.6
0.4
0.2
el. dens. (m^{-3})

Figure 5.

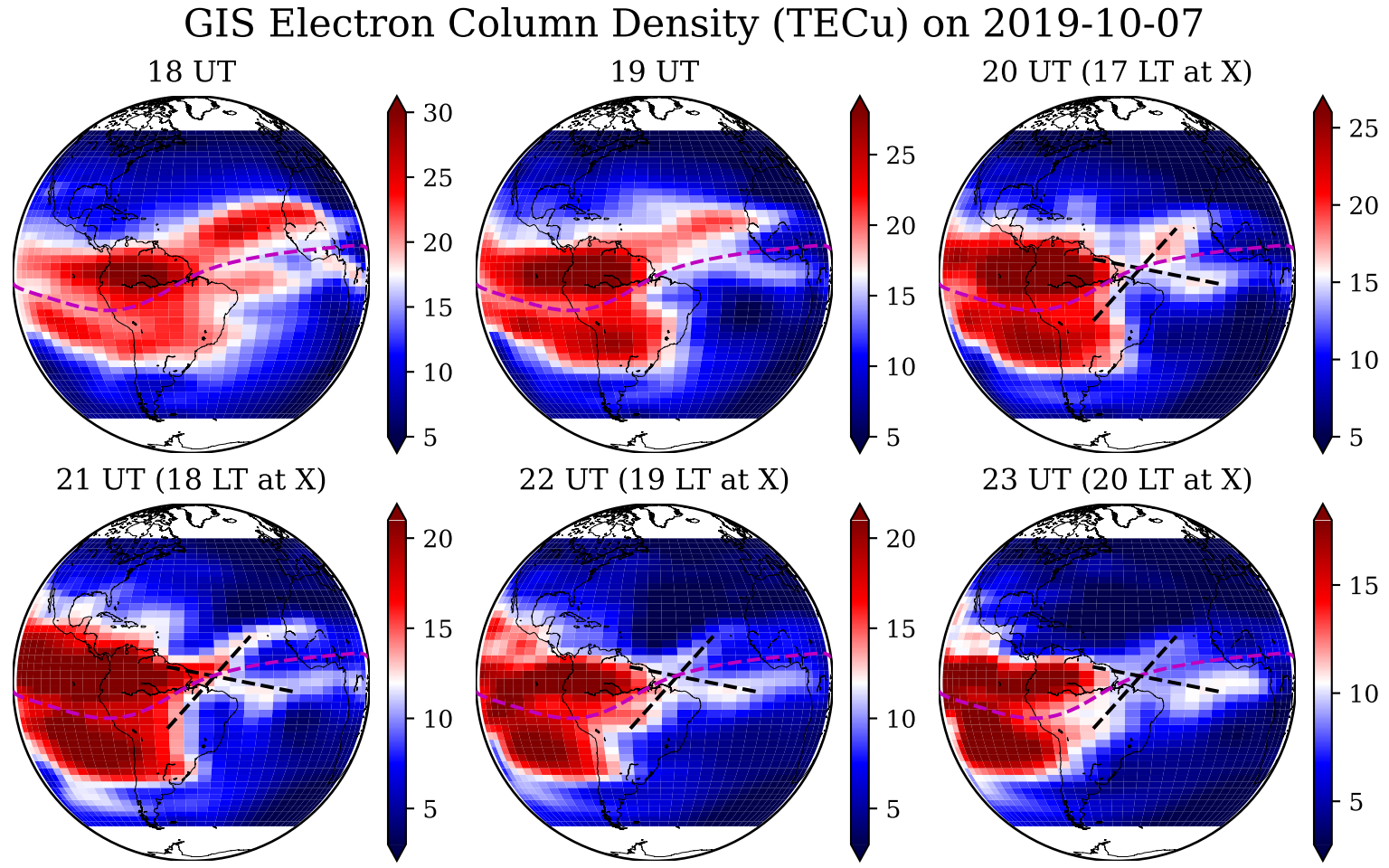
GIS Electron Column Density (TECu) on 2019-10-07
18 UT
19 UT
20 UT (17 LT at X)
21 UT (18 LT at X)
22 UT (19 LT at X)
23 UT (20 LT at X)
30
25
20
15
10
5